metals

MDPI

Article

Influence of Geometrical Design on Defect Formation of Commercial Al-Si-Cu-Mg Alloy Fabricated by High-Pressure Diecasting: Structural Observation and Simulation Validation

Warda Bahanan [1,†], Siti Fatimah [1,†], Dong-Ju Kim [2], I Putu Widiantara [1,*], Jee-Hyun Kang [1] and Young Gun Ko [1,*]

[1] School of Materials Science and Engineering, Yeungnam University, Gyeongsan 38541, Republic of Korea
[2] SeA Mechanics Co., Ltd., Gumi 39379, Republic of Korea
[*] Correspondence: iputuwidiantara89@yu.ac.kr (I.P.W.); younggun@ynu.ac.kr (Y.G.K.)
[†] These authors contributed equally to this work.

Abstract: Near-net-shaped metal products manufactured by high-pressure diecasting (HPD) encountered more or less critical failure during operation, owing to the development of micro-defects and structural inhomogeneity attributed to the complexity of geometrical die design. Because the associated work primarily relies on technical experience, it is necessary to perform the structural analysis of the HPDed component in comparison with simulation-based findings that forecast flow behavior, hence reducing trial and error for optimization. This study validated the fluidity and solidification behaviors of a commercial-grade Al-Si-Cu-Mg alloy (ALDC12) that is widely used in electric vehicle housing parts using the ProCAST tool. Both experimental and simulation results exhibited that defects at the interface of a compact mold filling were barely detected. However, internal micro-pores were seen in the bolt region, resulting in a 17.27% drop in micro-hardness compared to other parts, for which the average values from distinguished observation areas were 111.24 HV, 92.03 HV, and 103.87 HV. The simulation aligns with structural observations on defect formation due to insufficient fluidity in local geometry. However, it may underestimate the cooling rate under isothermal conditions. Thus, the simulation used in this work provides reliable predictions for optimizing HPD processing of the present alloy.

Keywords: Al alloy; high-pressure diecasting; structure; defect; ProCAST

check for updates

Academic Editor: Wenming Jiang

Received: 5 December 2024
Revised: 27 December 2024
Accepted: 2 January 2025
Published: 4 January 2025

Citation: Bahanan, W.; Fatimah, S.; Kim, D.-J.; Widiantara, I.P.; Kang, J.-H.; Ko, Y.G. Influence of Geometrical Design on Defect Formation of Commercial Al-Si-Cu-Mg Alloy Fabricated by High-Pressure Diecasting: Structural Observation and Simulation Validation. *Metals* **2025**, *15*, 42. https://doi.org/10.3390/met15010042

1. Introduction

High-pressure diecasting (HPD) is one of the most significant manufacturing techniques employed by the automotive industry for near-net-shaped aluminum (Al) products [1–3]. HPD is capable of producing thin-walled assemblies with a near-net form economically by injecting molten metal into a metal frame at high speed and solidifying it under high pressure [4,5]. This technique, however, generates intrinsic flaws, such as gas porosity in the resulting castings, which happens primarily due to the trapping of air in the molten metal as a result of the high-speed injection of liquid metal into the die chamber. Pores in casting are commonly identified as gas porosity and shrinkage porosity, which are detrimental as their presence negatively affects mechanical characteristics and pressure resistance [6–8]. Al series alloys, particularly Al-Si alloys, such as Al-Si-Cu and Al-Si-Mg, are extensively employed in the HPD industry because they have a distinctive combination of desired properties (high strength-to-weight ratio, high thermal and electrical conductivity, good formability, distinct corrosion behavior, and recycling potential) that are necessary in many areas of technology, especially in automobiles, where they successfully compete with steel and cast iron [1,9]. Several studies reported that the Al-Si series alloys produced via HPD demonstrate good comprehensive mechanical characteristics in the as-cast state [1]; however, some die-cast components were rejected at the foundry owing to casting failures including cold shut, stain, crack, shrinkage, and warpage [10].

The HPD procedure is fundamentally complicated in terms of geometrical design, and metallurgical and thermal variables, resulting in profound trial and error. According to Kong et al. [11], the soundness of cast components is greatly impacted by the combination of die temperature, the geometrical complexities of parts, liquid metal filling capacity, and die casting cooling rate. To address these challenges in casting manufacturing, numerical simulations using software such as ProCAST 2019.0 have become indispensable tools in design and optimization. A study by Andronov et al. [12], deploying ProCAST simulations for gearbox housing offers a practical way to overcome the challenges associated with full-mold printing. They successfully removed shrinkage porosity by improving part quality, regulating the temperature field, and optimizing heat exchange. Additionally, research conducted by Barkhudarov et al. [13] and Gunasegaram et al. [14] found that a slower melt moving speed in the shot sleeve can improve the mechanical qualities of the castings and minimize gas entrainment during the high-pressure diecasting process. The die cavity's solidification trends, heat transfer rates, and melt flow properties rely on the runner design and venting configuration.

Simulation-enabled casting is able to virtually model and evaluate the process, assisting in specific defect prediction and product development and hence decreasing work repetitions and increasing efficiency [15–17]. The existence of heat-induced defects, such as shrinkage flaws arising from unequal cooling temperatures, as seen in previous manufacturing tests using the conducting modulus method, can be prevented by adding modern cooling systems into the mold structure throughout the production process [18,19]. Moreover, the pouring temperature, semi-solid filling performance, and gating system design were explored to justify the microstructure of the critical zones in the components. The critical zones of Al alloy products were selected based on process parameters and numerical analysis [8,20]. In the present study, ProCAST was employed to simulate the HPD process of an Al-Si-Cu-Mg alloy for housing components in an electric vehicle (code name: DC box). The simulations identified problematic regions that require additional experimental examination.

Therefore, the present study focuses on conducting experimental observation on critical areas of a high-pressure die-casted Al-Si-Cu-Mg alloy, utilizing ProCAST software to simulate the process and determine regions of interest. The goal of this work is to deepen understanding of the casting process and its significant influence on the mechanical characteristics of the alloy. The simulation generated helpful information about the diecasting process, including the filling process, cooling rates, solidification time, and pore formation inside the casting. Following on from these findings, thorough experimental analyses were carried out, including microstructural observation using scanning electron microscopy (SEM), mechanical performance evaluation with microhardness testing, and casting defect visualization using 3D X-ray computed tomography. Furthermore, elevated reliability and efficiency of automotive components can be achieved through optimal design and manufacture.

2. Materials and Methods

2.1. Alloy and Mold

The material studied in this work was a die-cast ALDC12, whose elemental composition is provided in Table 1. The alloy was prepared by SeA Mechanics Co., Ltd., (Gumi, Republic of Korea). The base alloy was melted in a clay graphite crucible with an electric resistance furnace at 680 °C to effectively restrict hydrogen absorption. After each alloy addition, the melt was degassed for 15 min with argon using a commercial rotary degasser at a speed of 350 rpm for 5 min. After degassing, the melt was carefully skimmed, and a graphite heated cup was gently immersed in the liquid to prevent turbulence. This rigorous technique prevents oxide and air entrapment, yielding a high-quality finished alloy. The cups were soaked for about 20 s to attain the melting point. Upon removal, they were placed on an aluminum block to generate a temperature gradient during solidification.

Table 1. Chemical composition of die-cast ALDC12 matrix.

Element	Si	Cu	Mg	Al
Content (wt.%)	9.6	1.5	0.3	balance

A real casted sample (Figure 1a) and simulation-generated sample design with several view dimensions (Figure 1b) are shown below. The die frame was created to meet the needs of the automotive industry for housing boxes in electric vehicles. ProCAST 2019.0 was utilized to determine the efficacy of the design parameters considering spatial features. In terms of geometrical complexity and simulation aspects, the current work concentrated on three areas of interest: (i) thick parts (R1), (ii) bolt parts (R2), and (iii) corner parts (R3).

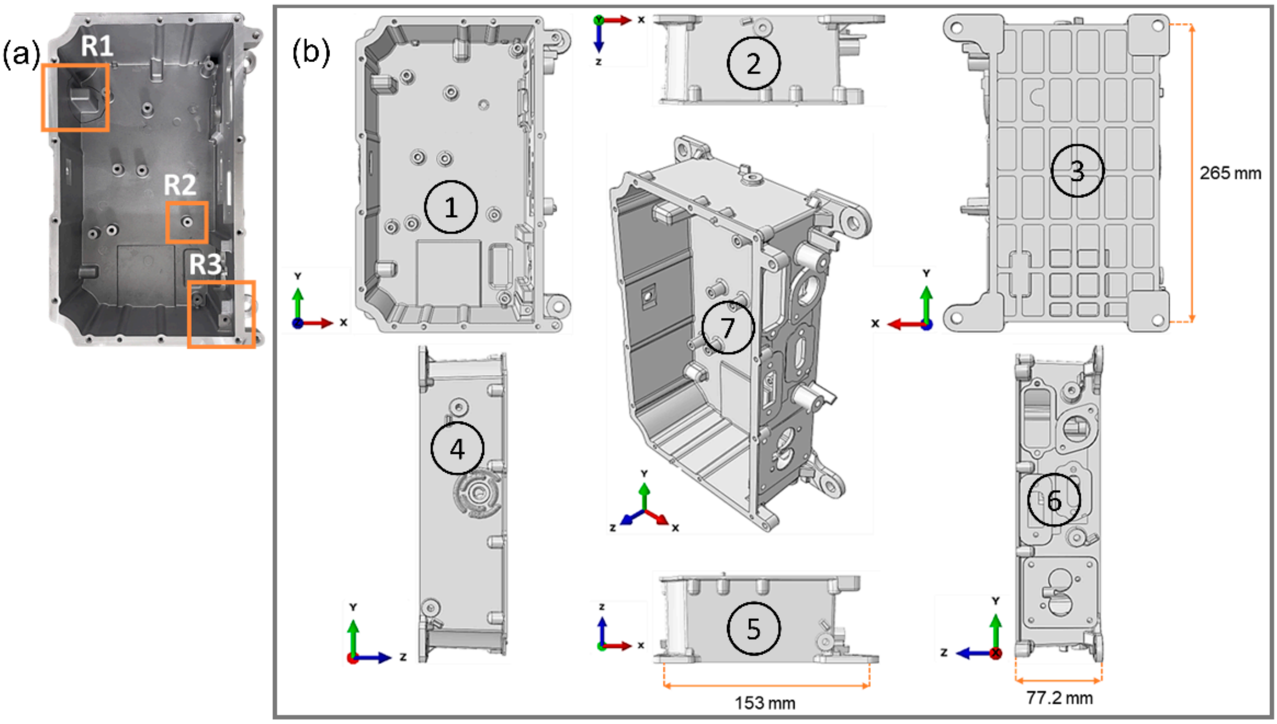

Figure 1. The view of real and simulation-generated samples from (1) front, (2, 4, 5, 6) sides, (3) back, and (7) tilted view. (**a**) real casted sample and (**b**) software-generated sample design.

2.2. Procast Simulation

ProCAST was developed by UES Software to model the casting of metals. ProCAST 2019.0 was employed in this study which is a comprehensive software package designed to enhance casting accuracy and yield in the foundry industry. ProCAST employs finite element analysis. In ProCAST, the Carreau–Yasuda material model was used. This model can be used for fitting a variety of complicated viscosity–shear rate curves. According to this model, the viscosity is related to the shear rate [21].

ProCAST is able to simulate various casting processes and is capable of describing the transport phenomena occurring in the different stages of casting, i.e., filling (fluid flow), solidification, die opening, part ejection and die closing. It should be noted that the solution of the fluid flow (momentum conservation via the Navier–Stokes equation) is only activated in the filling stages to improve computational efficiency. Whereas, the energy conservation is always computed throughout the process to update temperature distributions in the casting and die [22]. The ProCAST model incorporates the key process boundary conditions and material properties [22]. Validation against data measured on the production process has demonstrated the model's accuracy.

2.3. High-Pressure Diecasting (HPD)

Before proceeding with the HPD procedure, distinct parameters (Table 2) were introduced into the simulation environment. The experiment was carried out by applying the conditions listed below.

Table 2. The parameter of high-pressure diecasting for experiment and simulation.

Filling Temperature (°C)	Die Temperature (°C)	Shot Speed (m/s)	Pressure (MPa)
660	230	0.25~2.0	50

2.4. Microstructure Observation and Mechanical Testing

A scanning electron microscope (SEM, Hitachi S-4800 at an operating voltage of 15 kV) was used to observe both the grain and defects found in the local region that might suffer from the insufficient solidification as predicted by ProCAST. To attain high feasibility in the structural analysis, the same position was be taken from five different products prepared under identical manufacturing conditions. The representative observation will be provided in the next section. For SEM observation, the surface of the sample was mechanically polished and chemically etched using a two-step process: first, using a solution consisting of 20 mL of CrO_3 and 12.5 mL of HNO_3, followed by the application of a second solution consisting of 1.25 mL of H_2O, 15 mL of HCl, 7.5 mL of HNO_3, and 1.25 mL of HF. Moreover, the X-ray microscope (Xradia 620 Versa, Carl Zeiss Germany, with a spatial resolution of 0.5 µm) was used to characterize the 3-dimensional structure of the sample in order to understand the spatial population of the casting defect in a qualitative manner.

For mechanical testing on the surface after fine polishing, a series of the micro-Vickers hardness tests (Wilson Instrument, Norwood, MA, USA, Vickers 402 MVD using 0.5 kg of indentation load for 10 s of dwell time) were performed under the restricted condition that maintained 0.2 µm as a gap between indentations in order to inhibit the physical influence from the previous indentation. Also, a series of indentations were made and the average value of the data will be provided.

3. Results

As the nature of the HPD microstructure is decorated by defects, the present work scrutinized the defect formation by simulating the fluidity and solidification behavior considering geometrical differences. Through this approach, the formation of defects can be understood and better designs of the sample can be suggested for commercialization.

3.1. Simulation Analysis

From the ProCAST simulation, the filling percentage of the HPD process for 60%, 80%, and 100% are shown in Figure 2a (front view) and Figure 2b (side view). The filling process where the feedstock (red color coded) moved through the y direction to fill the mold (gray color coded). Although some parts of the sample showed imperfect filling behavior at 60% (front), the feedstock completely filled the whole mold at 100% progress.

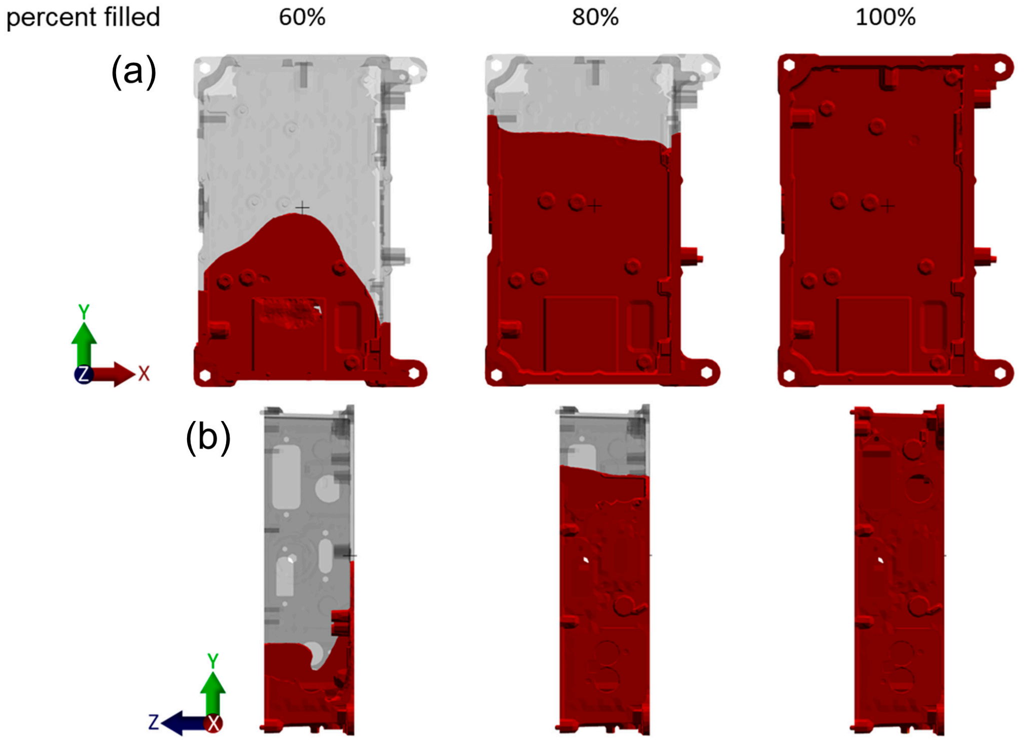

Figure 2. Filling progress from (**a**) front and (**b**) side view within the filling percentage of 60%, 80%, and 100% from left to right.

Using ProCAST software, three different simulations were carried out, namely, cooling rate, solidification time, and micro-defect generation, as shown in Figure 3a–c, respectively. Each feedstock is colored in accordance with the cooling rate (in K/s) and solidification time (in second), with the color scale right beside the simulated object. In general, cooling rate was uniform throughout the entire mold under isothermal conditions (Figure 3a). Interestingly, despite the uniform cooling rate, a number of regions showed local solidification behavior such that the two regions showed higher solidification times (blue color coded) or solidified later than the other region (violet color coded) (Figure 3b). The results inferred that the difference in solidification time was obvious in region R1 and R3, whilst it was hardly found in region R2. Lastly, the simulation of pore presence showed a number of regions developing pores at the end of the filling process (highlighted by using solid and dashed lines), which were populated near to the corner and bolt regions.

Based on the simulation results, three different regions, namely, R1 (thick part), R2 (bolt region), and R3 (corner part), which were designed for investigation, showed distinct solidification times for R1 and R3, indicating that geometrical differences governed the solidification behavior. This criterion can be employed to predict the risk of shrinkage failures. The longest casting solidification duration suggests the possibility of cumulative shrinkage, which could result in the occurrence of future voids. This is typically seen in places where the walls are thicker [12]. On the other hand, internal micro-defects were also found in the bolt region of R2, inferring that some factors beyond solidification behavior influence defect generation. In addition, because R2 is a bolt part considered to have a complex geometry and as its role is considered to be more significant for the product application compared to the other parts that contain pores, R2 will be investigated as a representative of region with pores (Figure 3c, solid lines).

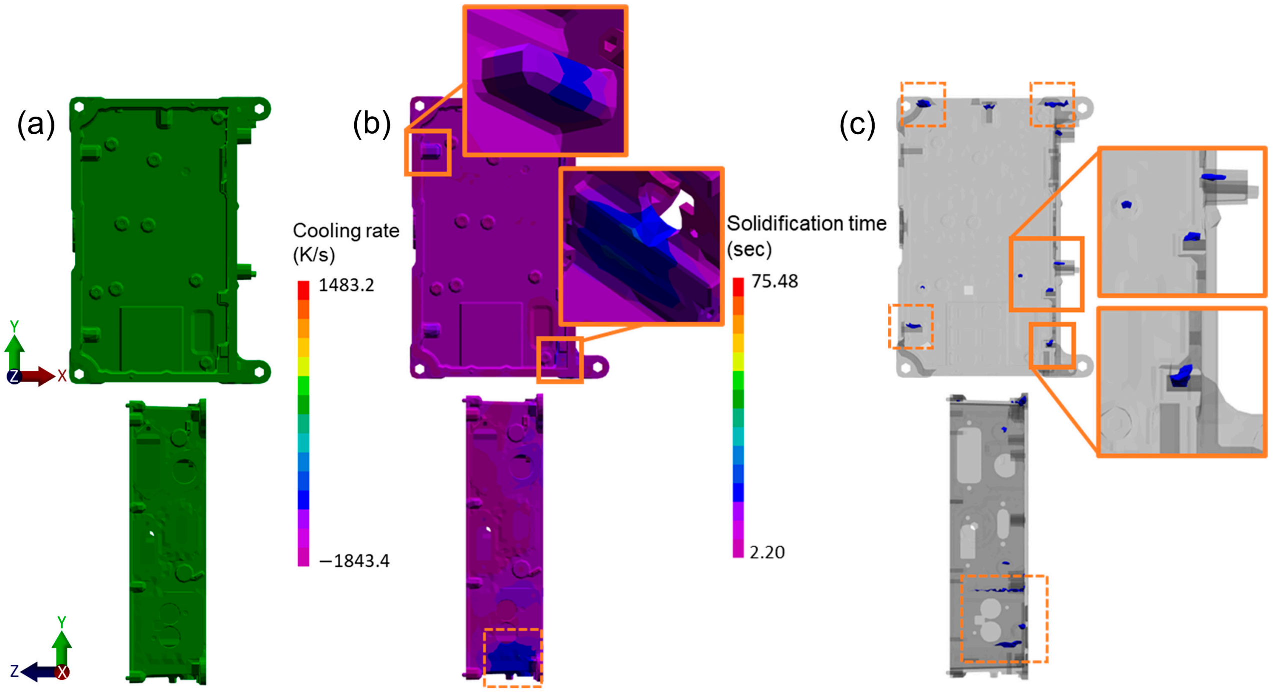

Figure 3. ProCAST modelling results for the (**a**) cooling rate, (**b**) solidification time, and (**c**) pore presence.

3.2. Microstructure

Microstructural observation was carried out for R1, R2, and R3 (Figure 4). In general, the microstructure revealed a mixture of α-Al phase (the darker part) and eutectic phase (the lighter part), which can be seen clearly at higher magnification. The eutectic characteristics, commonly observed in Al-Si alloys, are more obvious in Al-Si-Cu owing to the relatively high liquidous temperature [23]. The formation of such phases would increase the surface inhomogeneity and accordingly alter the surface properties. For example, whilst the eutectic phase might increase the strength and hardness, the ductility of the materials might be dropped [23,24]. It is worth noting that the fraction of α-Al in R3 seemed to be higher than in R1 and R2.

In terms of internal micro-defects, porosity percentage and average pore size for each region are shown in the diagram (Figure 4). According to Zhang et al. [19], porosity does affect mechanical performance, but more significantly, it also depends on the size and morphology of the porosities. A uniform distribution of porosity will reduce potential negative effects on the sample's performance. The graph showing the highest porosity percentage and average pore size are both occupied by R2 (16.06% and 7.4 micron, respectively). On the other hand, micro-pores were hardly observed in R1 and R3. Qualitatively presented in the graph, for porosity percentage and average pore size, R1 had 2.78% and 2.8 micron, and R2 owned 6.86% and 4.1 micron, respectively. Previous research has suggested that holes in casting products might be detected as either gas pores with a spherical shape or shrinkage pores with an irregular form surrounded by dendritic borders [7,25]. It is suggested that the pores found in region R2 of Figure 4 were shrinkage pores which would be formed due to the effect of shrinkage and the lack of feeding during solidification. On the other hand, the gas pores would be induced by gas trapping and insoluble gases like hydrogen [7]. Interestingly, the micro-pores found in R2 populated the vicinity of the boundary, viz. the interface between α-Al and the eutectic phase, α-Al and α-Al, and the eutectic phase and eutectic phase.

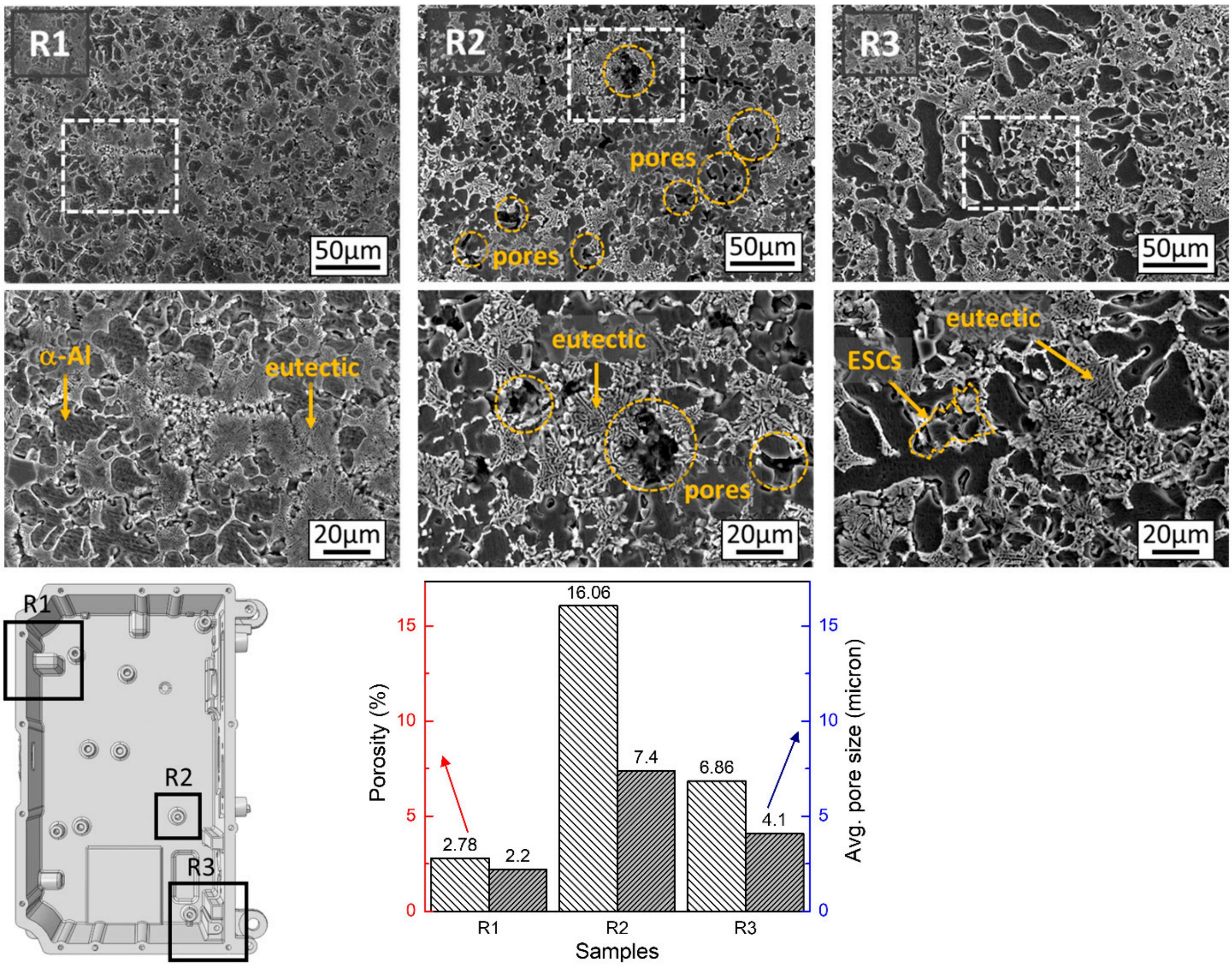

Figure 4. Microstructure results for the thick part (R1), bolt part (R2), and corner part (R3). Lower figures showing the magnification view of the white square on the upper side. The presence of ESCs (externally solidified crystals) can be seen in the corner body (R3). The porosity percentage and average pore size (micron) are presented in the histogram.

In addition, externally solidified crystal (ESC) was detected on R3, which indicated a certain degree of surface defect [24]. The nucleation of ESCs takes place at the shot sleeve surface due to the gradient temperatures between the melt and shoot sleeve. ESCs were typically responsible for microstructural heterogeneity. The weighted average of the segregation band width and the volume percent porosity may be expected to determine the strength and overall deformation behavior of the HPD alloy because the structural heterogeneity varies the grain size between the central area and the surface [26]. The shrinkage pores might be formed among the boundaries of ESC, which further increases the surface inhomogeneity of the materials leading to the uneven distribution of hardness.

A dedicated analysis of the bolt area containing a large fraction of pores in R2 was carried out using 3D X-ray computed tomography as well as elemental analysis using XRD (Figure 5). The part around the bolt was investigated and it can be seen that a number of voids were detected and some were clustered to form pores. Based on previous investigation, the rate of cooling influences how much porosity exists. Higher solute and hydrogen concentrations are found close to the dendritic as the solute diffusion layer because solutes and hydrogen have a shorter time to diffuse away into the liquid from the dendrite at rapid cooling rates [7]. Elemental analysis was carried out to detect the existence of Al, Si, Cu and Mg. Based on the results, R2 revealed the morphology of the pore (pit black area) which is located at the α-Al phase where the elements were not detected.

Furthermore, the eutectic phase was a mixture of both Al and Si while α-Al consisted of nearly pure Al. In addition, Cu and Mg elements were detected in relatively small fractions as compared to Al and Si.

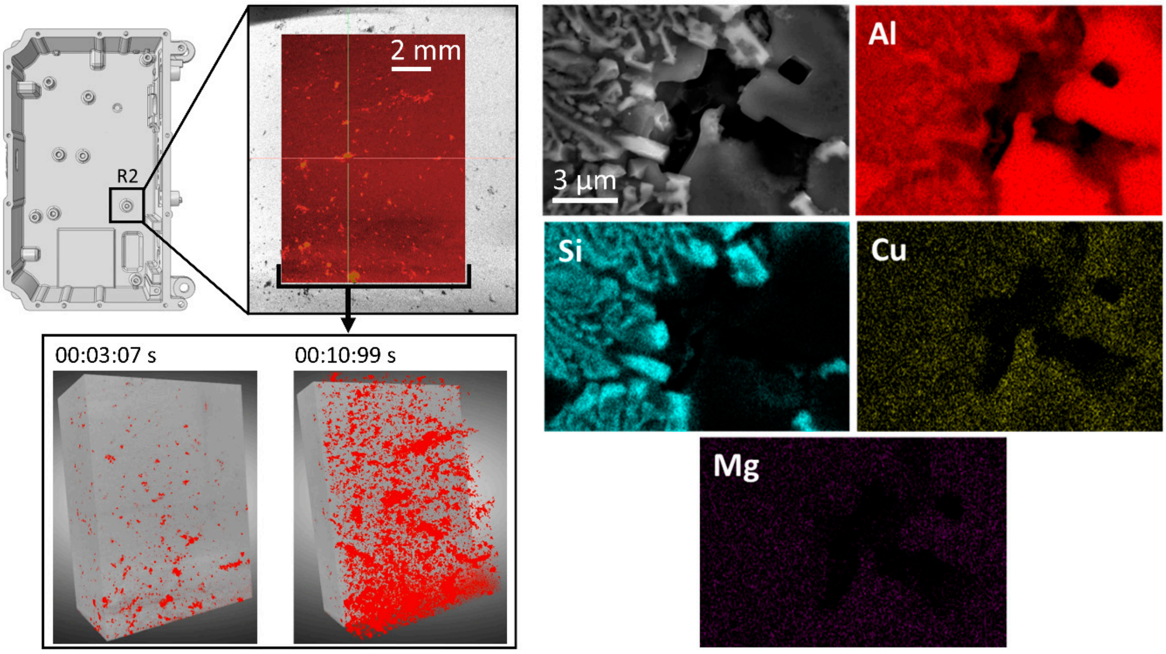

Figure 5. 3D morphology and elemental analysis of bolt area (R2).

Mechanical assessment using Vickers' microhardness was carried out on all samples. A series of indentations were carried out at 17 points around R1, R2, and R3 (Figure 6a). A distance of 0.2 μm was selected as the minimum distance between indentations in order to avoid any effect from the neighboring indentation mark. The tendency for hardness was R1 > R3 > R2. It can be seen that the error bar was the highest for R2, which suggests non-uniform mechanical properties in this particular part. The average micro-hardness values from the distinguished observation areas (R1, R2, and R3) were found to be 111.24 HV, 92.03 HV, and 103.87 HV, respectively. However, internal micro-pores were seen in the bolt region, resulting in a 17.27% drop in micro-hardness compared to the other parts. Figure 6b shows the characteristics of the indentation marks for R1, R2, and R3.

The indentation mark size was inversely proportional to the calculated hardness, where the sizes were R2 > R3 > R1, which can be correlated with the grain size and the presence of micro-defects due to different fluidity. The indentation size decreases with increasing hardness and is fundamentally correlated to the material's resistance to plastic deformation. Moreover, the indentation mark of R1 was finely shaped as compared to that in the other parts. The indentation mark in R3 had a slight curve in its side, suggesting a ductile manner rather than a hard manner. More importantly, R2 not only showed a much coarser indentation size but it also showed a formation of fracture defect.

In summary, the present strategy produced a sample of housing boxes via HPD with relatively dense microstructures, no macro-defects, and an average pore size of ~7.4 micron in the bolt regions, which is significantly smaller than the ~10 micron reported in previous works utilizing the same method on Al-Si-Mg alloy for shock tower components in automobiles [27]. Moreover, lowering the thickness of the HPD-ed sample by less than 1 mm resulted in the formation of macro-defects such as blisters on the Al-Si-Mg for electronic cases [28]. While no significant defects were observed in the present sample, Matejka et al. [29] documented that hotspots were detected on the center body of the Al-Si-Cu following HPD due to the presence of oxides produced by turbulence flow which would suppress the venting process and result in trapped bubbles. The defects are characterized by a spherical shape, and possibly by a combination of mechanisms of bubble and shrinkage formation. The present strategies were found to be more effective in preventing the formation of macro-defects such as blisters, while serving at a relatively high hardness of 92~111 HV, which was much higher than those of 72~75 HV on HPD-ed Al 6061 [30].

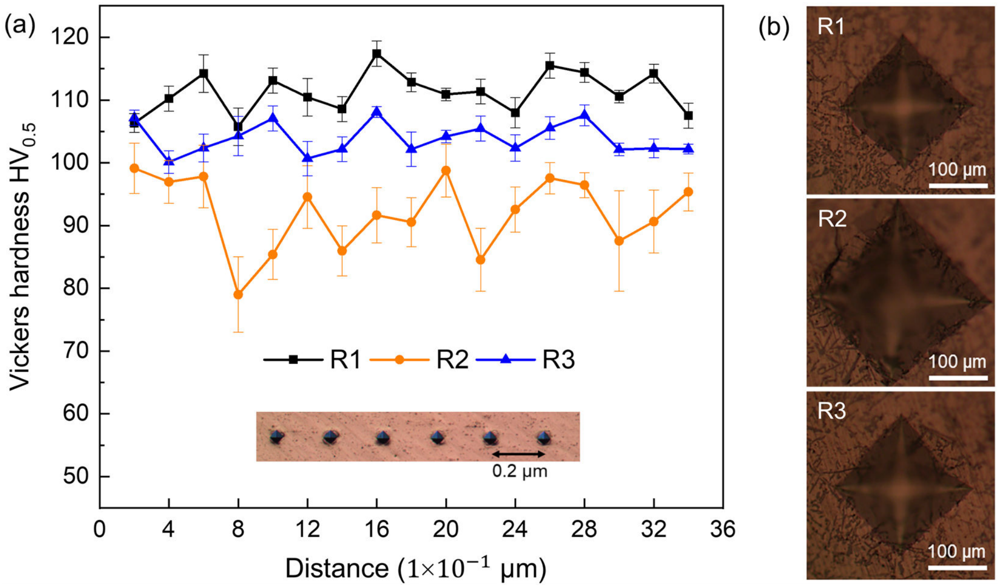

Figure 6. (**a**) Microhardness distribution (obtained using 0.5 kgf) and (**b**) micrograph of the indentation marks on the regions of interest in the final product corresponding to thick part (R1), bolt part (R2), and corner part (R3).

4. Discussion

The ALDC12 aluminum alloy is a hypoeutectic alloy that solidifies in two distinct stages, exhibiting mushy solidification behavior [31]. In the primary phase, globular structures were formed. In the second stage, the remaining liquid solidified into a eutectic mixture, resulting in a characteristic microstructure comprising primary phase regions surrounded by eutectic material. Simulation results demonstrated a uniform cooling rate across the entire sample under isothermal conditions (as indicated by consistent color distribution), which explains the observed microstructure of mushy solidification in all three analyzed regions.

The formation of pores and the degree of porosity was strongly related to the solidification shrinkage (β), volume of the gas, pressure of the gas during solidification (P), proportion of gas that does not enter the pores (φ), volume of the liquid in the casting cavity (V^*), volume of the casting cavity (V_c), amount of gas during casting (v),solubility limit of gas in the solid phase (v^*), density of the liquid alloy (ρ), and the temperature of the gas (T), which was formulated below [32].

$$\%P = \frac{\beta V^*}{V_C} + \left(\varphi \frac{T\,\rho L}{(237\ K)\ P}\right)(v - v^*)$$

While the first half of the equation describes the relationship of porosity as the results of solidification shrinkage, the second half describes the porosity caused by gas trapping including those from physical entrapment, lubricant breakdown, and gas dissolved in alloy. Therefore, the porosity caused by gas trapping and that caused by solidification shrinkage offers meaningful information for understanding the feedstock behavior during casting, which is investigated further by ProCAST.

The formation of pores in R2, as shown in the microstructural figures in the results section, was examined with regard to the modelling capabilities of ProCAST. In this software, feedstock fluidity was influenced by shear effects. Observing the filling pattern, the feedstock flowed from the bottom to the top and then encountered the bolt geometry. According to Bilovol et al. [21], ProCAST accurately predicts the position of weld lines, which occur when two melt fronts meet after being split by the hollow bolt geometry. This accuracy surpasses that of C-Mold simulations, which failed to account for the shear effects between the two streams, thereby predicting identical positions for the melt fronts with no gradient between them [33]. ProCAST, by contrast, successfully simulates the weld line position, which coincided with the pore formation observed in R2, which was shown in the schematic illustration in Figure 7a. This suggests that ProCAST predicted pore formation based on the estimated weld line locations, consistent with the well-known structural weakness of weld lines. Interestingly, the size of the forecast pores in the upper bolt was larger than those in the lower bolt, likely due to a greater gradient between the two feedstock streams at the upper bolt. In accordance with Figure 4, where ESC was formed in R3, weld line formation showed more potential in generating pores that negative effects on the mechanical properties such as hardness. The simulation also shows that the solidification of R1 and R3 occurs later than that of R2, despite similar cooling rates across all regions. While reducing solidification time is generally associated with smaller and fewer pores [34], R2, with a shorter solidification time, exhibited more pores than R1 and R3, further supporting the hypothesis that weld line formation influences pore distribution.

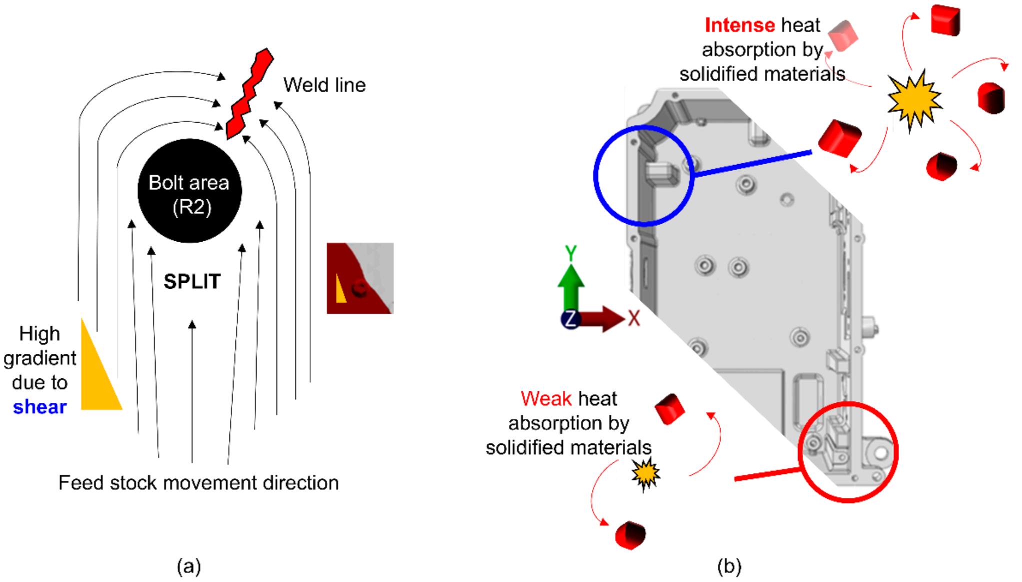

Figure 7. Schematic illustration of (**a**) weld formation around R2 and (**b**) different cooling rates at different positions.

The presence of internal micro-defects such as micro-pores in R2 which are located mainly in the interface boundaries between grains or phases are attributed to several factors: (i) Solidification shrinkage, where α-Al matrix solidifies faster and leaves the impurities in the vicinity of the boundary, forming micro-defects as the eutectic phase solidifies later. As the eutectic phase shrinks later, the voids could be made as the liquids could not fill the shrinkage region [9,35]. (ii) Different thermal expansion coefficients would generate stress and cause interface separation [36,37]. (iii) A high cooling rate of ~70 K/s would induce incomplete bonding between the matrix and the eutectic phase, contributing to defect formation [38]. In addition, a higher cooling rate of 103~105 K/s might induce the formation of granular Si instead of dendritic structure [39].

Microstructural observations reveal a higher fraction of α-Al (primary aluminum) in R3 compared to R1 and R2. Typically, α-Al grain size decreases with higher cooling rates [40]. However, despite the simulation indicating similar cooling rates across all regions, R3 exhibits coarser α-Al grains. This rules out a temperature drop due to latent heat release during Al-Si eutectic solidification, as no fold defects were detected at the surface [41]. Instead, it suggested another factor affecting α-Al grain morphology. Liao et al. [42] proposed that as feedstock advances toward the sample's center, cooling rates increase due to the enhanced heat absorption capacity of the solidified material. In this case, the melts positioned around R3 (positioned closest to the gate) were likely to have the smallest cooling rates, compared to R1 and R2, which allowed more time for α-Al grain to grow in R3 as compared to that in R1 and R2. A schematic illustration for this is given in Figure 7b.

In this study, casting parameters were carefully optimized through trial and error to remain within critical thresholds, as exceeding these limits can result in gas-related defects and excessive porosity [43]. However, the issues encountered in this study could not be resolved through parameter adjustments alone where a higher temperature and pressure of 660 °C and 50 MPa, respectively, might be needed to ease the formation of weld line. The best way to resolve this issue is to carry out design modifications. This research highlights the importance of using casting simulations, such as those conducted with ProCAST, to predict pore formation and prevent defects. While no specific geometry was deemed problematic, the location of certain features relative to the casting gate significantly influenced defect formation. Overall, the casting parameters employed in this study are recommended, as they resulted in the absence of surface defects or other significant issues.

5. Conclusions

The present work systematically conducted experimental observation on three distinctive regions that were assigned to be R1 (thick part), R2 (bolt region), and R3 (corner part), of a high-pressure diecasted Al-Si-Cu-Mg alloy, utilizing ProCAST software to simulate the process. The following concluding remarks were drawn:

1. ProCAST successfully determined the critical areas to be thoroughly investigated through the filling process, cooling rate, solidification time, and pinpointed location with pore occupation. The simulation accurately indicated interior porosity developed near the bolt area by accounting for feedstock behavior and the formation of weld lines in the vicinity of the bolt geometry.
2. The highest porosity percentage and average pore size belonged to R2 with 16.06% and a 7.4-micron pore size. Most of the micro-pore formation found on the microstructure is shrinkage porosity that was attributed due to the complexity of the geometry and thicker wall.
3. This simulation was in line with pore-decorated microstructures and the non-uniform Vickers' microhardness analysis, mainly in R2. The existence of pores dominantly cut down the mechanical performance which resulted in a 17.27% drop in observation areas R1, R2, and R3, which owned the value of 111.24 HV, 92.03 HV, and 103.87 HV.
4. The simulation underestimated the role of solidified material on the cooling rate, which should have altered the morphology of the α-Al phase. Nevertheless, the results underscore the utility of ProCAST as a potential tool for simulating the die-casting process.

Author Contributions: Conceptualization, W.B., S.F., I.P.W., Y.G.K. and J.-H.K.; methodology, W.B., S.F., I.P.W. and Y.G.K.; software, W.B., I.P.W. and D.-J.K.; validation, W.B., S.F., I.P.W. and Y.G.K.; formal analysis, S.F., D.-J.K. and J.-H.K.; investigation, W.B. and S.F.; resources, D.-J.K. and Y.G.K.;

data curation, D.-J.K.; writing—original draft preparation, W.B. and S.F.; writing—review and editing, W.B., S.F., I.P.W., Y.G.K. and J.-H.K.; visualization, I.P.W., D.-J.K., J.-H.K. and Y.G.K.; supervision, J.-H.K., I.P.W. and Y.G.K.; project administration, Y.G.K.; funding acquisition, Y.G.K. All authors have read and agreed to the published version of the manuscript.

Funding: This work was supported by Industry-University-Institute Joint R&D Project in conjunction with SeA Mechanics Co., Ltd., funded by Ministry of SMEs and Startups (#S3159832).

Data Availability Statement: The original contributions presented in this study are included in the article. Further inquiries can be directed to the corresponding author.

Conflicts of Interest: Author Dong-Ju Kim was employed by the company SeA Mechanics Co., Ltd. The remaining authors declare that the research was conducted in the absence of any commercial or financial relationships that could be construed as a potential conflict of interest.

References

1. Trudonoshyn, O.; Rehm, S.; Randelzhofer, P.; Körner, C. Improvement of the High-Pressure Die Casting Alloy Al-5.7Mg-2.6Si-0.7Mn with Zn Addition. *Mater. Charact.* **2019**, *158*, 109959. [CrossRef]
2. Otarawanna, S.; Gourlay, C.M.; Laukli, H.I.; Dahle, A.K. Microstructure Formation in AlSi4MgMn and AlMg5Si2Mn High-Pressure Die Castings. *Metall. Mater. Trans. A Phys. Metall. Mater. Sci.* **2009**, *40*, 1645–1659. [CrossRef]
3. Stemper, L.; Mitas, B.; Kremmer, T.; Otterbach, S.; Uggowitzer, P.J.; Pogatscher, S. Age-Hardening of High Pressure Die Casting AlMg Alloys with Zn and Combined Zn and Cu Additions. *Mater. Des.* **2019**, *181*, 107927. [CrossRef]
4. Hu, Z.; Wan, L.; Wu, S.; Wu, H.; Liu, X. Microstructure and Mechanical Properties of High Strength Die-Casting Al-Mg-Si-Mn Alloy. *Mater. Des.* **2013**, *46*, 451–456. [CrossRef]
5. Zhou, Y.; Guo, Z. Effect of Runner Design on the Externally Solidi Fi Ed Crystals in Vacuum Die-Cast Mg-3.0Nd-0.3Zn-0.6Zr Alloy. *J. Mater. Process. Technol.* **2019**, *267*, 366–375. [CrossRef]
6. Niu, X.P.; Hu, B.H.; Pinwill, I.; Li, H. Vacuum Assisted High Pressure Die Casting of Aluminium Alloys. *J. Mater. Process. Technol.* **2000**, *105*, 119–127. [CrossRef]
7. Gu, C.; Lu, Y.; Luo, A.A. Three-Dimensional Visualization and Quantification of Microporosity in Aluminum Castings by X-Ray Micro-Computed Tomography. *J. Mater. Sci. Technol.* **2021**, *65*, 99–107. [CrossRef]
8. Zeng, J.; Zhang, W.; Guo, T.; Lou, Y.; Wang, W.; Zhao, Z.; Wang, C. Numerical and Experimental Analysis of Dual-Beam Laser Polishing Additive Manufacturing Ti6Al4V. *Micromachines* **2023**, *14*, 1765. [CrossRef]
9. Ma, Y.; Yu, W.; Yuan, Z.; Ma, C.; Chen, W.; Wu, M.; Xiong, S. 3D Characterization of Pores Expansion Behavior in High Pressure Die Castings during Heat Treatment. *Mater. Charact.* **2023**, *197*, 112710. [CrossRef]
10. Bharambe, C.; Jaybhaye, M.D.; Dalmiya, A.; Daund, C.; Shinde, D. Analyzing Casting Defects in High-Pressure Die Casting Industrial Case Study. *Mater. Today Proc.* **2023**, *72*, 1079–1083. [CrossRef]
11. Kong, L.X.; She, F.H.; Gao, W.M.; Nahavandi, S.; Hodgson, P.D. Integrated Optimization System for High Pressure Die Casting Processes. *J. Mater. Process. Technol.* **2008**, *201*, 629–634. [CrossRef]
12. Andronov, V.; Pitrmuc, Z.; Zajíc, J.; Šotka, P.; Beránek, L.; Bock, M. Conformal Cooling as a Support Tool for Eliminating Local Defects in High-Pressure Die Casting Series Production. *Prog. Addit. Manuf.* **2024**. [CrossRef]
13. Barkhudarov, M.R.; President, V. Computer Modeling Simulation Minimizing Air Entrainment in a & during Slow-Shot Stage. *Die Cast. Eng.* **2009**, *53*, 34–37.
14. Gunasegaram, D.R.; Givord, M.; O'Donnell, R.G.; Finnin, B.R. Improvements Engineered in UTS and Elongation of Aluminum Alloy High Pressure Die Castings through the Alteration of Runner Geometry and Plunger Velocity. *Mater. Sci. Eng. A* **2013**, *559*, 276–286. [CrossRef]
15. Fu, M.W.; Yong, M.S. Simulation-Enabled Casting Product Defect Prediction in Die Casting Process. *Int. J. Prod. Res.* **2009**, *47*, 5203–5216. [CrossRef]
16. Lee, J.H.; Park, S.J.; Yang, J.; Moon, S.K. Crack Control in Additive Manufacturing by Leveraging Process Parameters and Lattice Design. *Micromachines* **2024**, *15*, 1361. [CrossRef]
17. Karg, M.C.H.; Ahuja, B.; Wiesenmayer, S.; Kuryntsev, S.V.; Schmidt, M. Effects of Process Conditions on the Mechanical Behavior of Aluminium Wrought Alloy EN AW-2219 (AlCu6Mn) Additively Manufactured by Laser Beam Melting in Powder Bed. *Micromachines* **2017**, *8*, 23. [CrossRef]
18. Kwon, H.J.; Kwon, H.K. Computer Aided Engineering (CAE) Simulation for the Design Optimization of Gate System on High Pressure Die Casting (HPDC) Process. *Robot. Comput. Integr. Manuf.* **2019**, *55*, 147–153. [CrossRef]
19. Zhang, Y.; Lordan, E.; Dou, K.; Wang, S.; Fan, Z. Influence of Porosity Characteristics on the Variability in Mechanical Properties of High Pressure Die Casting (HPDC) AlSi7MgMn Alloys. *J. Manuf. Process.* **2020**, *56*, 500–509. [CrossRef]

20. Ren, S.; Wang, F.; Sun, J.; Liu, Z.; Mao, P. Gating System Design Based on Numerical Simulation and Production Experiment Verification of Aluminum Alloy Bracket Fabricated by Semi-Solid Rheo-Die Casting Process. *Int. J. Met.* **2022**, *16*, 878–893. [CrossRef]
21. Bilovol, V.V.; Kowalski, L.; Duszczyk, J.; Katgerman, L. Comparison of Numerical Codes for Simulation of Powder Injection Moulding. *Powder Metall.* **2003**, *46*, 55–60. [CrossRef]
22. Ou, J.; Wei, C.; Maijer, D.; Cockcroft, S.; Zhang, Y.; Chen, Z.; Zhu, Z. Modelling of an Industrial Die Casting Process for the Production of Aluminum Automotive Parts. *IOP Conf. Ser. Mater. Sci. Eng.* **2020**, *861*, 012030. [CrossRef]
23. Timelli, G.; Fabrizi, A. The Effects of Microstructure Heterogeneities and Casting Defects on the Mechanical Properties of High-Pressure Die-Cast AlSi9Cu3(Fe) Alloys. *Metall. Mater. Trans. A Phys. Metall. Mater. Sci.* **2014**, *45*, 5486–5498. [CrossRef]
24. Sun, Q.; Yuan, L.; Tong, X.; Wang, J.; Wang, X.; Peng, L.; Ding, W. Formation Mechanism of the Microstructural Heterogeneity in a Die-Cast Al-Mg-Si Alloy and Its Effect on Mechanical Properties. *Mater. Charact.* **2024**, *213*, 114004. [CrossRef]
25. Dong, X.; Yang, H.; Zhu, X.; Ji, S. High Strength and Ductility Aluminium Alloy Processed by High Pressure Die Casting. *J. Alloys Compd.* **2019**, *773*, 86–96. [CrossRef]
26. Jiang, Y.; Zheng, H.; Liu, F.; Zhao, H. Effect of Zn Addition on the Microstructural Heterogeneity and Mechanical Properties of Vacuum-Assisted High-Pressure Die Casting Al–Si–Mg–Cu Alloys. *Adv. Eng. Mater.* **2023**, *25*, 2201457. [CrossRef]
27. Cantú-Fernández, D.S.; Taha-Tijerina, J.J.; González, A.; Hernández, P.G.; Quinn, B. Mechanical Properties of a Structural Component Processed in High-Pressure Die Casting (HPDC) with a Non-Heat-Treated Aluminum Alloy. *Metals* **2024**, *14*, 369. [CrossRef]
28. Gomes, R.; Soares, G.; Madureira, R.; Silva, R.P.; Silva, J.; Neto, R.; Reis, A.; Fernandes, C. Development of Heat Treatments for Structural Parts in Aluminium Alloys Produced by High-Pressure Die Casting (HPDC). *Metals* **2024**, *14*, 1059. [CrossRef]
29. Matejka, M.; Bolibruchová, D.; Podprocká, R. The Influence of Returnable Material on Internal Homogeneity of the High-pressure Die-cast $AlSi_9Cu_3$(Fe) Alloy. *Metals* **2021**, *11*, 1084. [CrossRef]
30. Agarwal, M.; Srivastava, R. Influence of Processing Parameters on Microstructure and Mechanical Response of a High-Pressure Die Cast Aluminum Alloy. *Mater. Manuf. Process.* **2019**, *34*, 462–472. [CrossRef]
31. Qi, M.; Kang, Y.; Qiu, Q.; Tang, W.; Li, J.; Li, B. Microstructures, Mechanical Properties, and Corrosion Behavior of Novel High-Thermal-Conductivity Hypoeutectic Al-Si Alloys Prepared by Rheological High Pressure Die-Casting and High Pressure Die-Casting. *J. Alloys Compd.* **2018**, *749*, 487–502. [CrossRef]
32. Vinarcik, E.J. *High Integrity Die Casting Processes*; John Wiley & Sons, Inc.: Hoboken, NJ, USA, 2002; ISBN 0471275468.
33. Oliaei, E.; Heidari, B.S.; Davachi, S.M.; Bahrami, M.; Davoodi, S.; Hejazi, I.; Seyfi, J. Warpage and Shrinkage Optimization of Injection-Molded Plastic Spoon Parts for Biodegradable Polymers Using Taguchi, ANOVA and Artificial Neural Network Methods. *J. Mater. Sci. Technol.* **2016**, *32*, 710–720. [CrossRef]
34. Caton, M.J.; Jones, J.W.; Allison, J.E. The Influence of Heat Treatment and Solidification Time on the Behavior of Small-Fatigue-Cracks in a Cast Aluminium Alloy. *Mater. Sci. Eng. A* **2001**, *314*, 81–85. [CrossRef]
35. Zhang, T.; Yu, W.; Ma, C.; Zhou, Y.; Xiong, S. Effects of Runner Design and Pressurization on the Microstructure of a High-Pressure Die Cast Mg-3.0Nd-0.3Zn-0.6Zr Alloy. *Int. J. Miner. Metall. Mater.* **2022**, *29*, 1310–1316. [CrossRef]
36. Liu, R.; Zheng, J.; Godlewski, L.; Zindel, J.; Li, M.; Li, W.; Huang, S. Influence of Pore Characteristics and Eutectic Particles on the Tensile Properties of Al–Si–Mn–Mg High Pressure Die Casting Alloy. *Mater. Sci. Eng. A* **2020**, *783*, 139280. [CrossRef]
37. Jiao, X.Y.; Wang, P.Y.; Liu, Y.X.; Wang, J.; Liu, W.N.; Wan, A.X.; Shi, L.J.; Wang, C.G.; Xiong, S.M. Fracture Behavior of a High Pressure Die Casting AlSi10MnMg Alloy with Varied Porosity Levels. *J. Mater. Res. Technol.* **2023**, *25*, 1129–1140. [CrossRef]
38. Karakoc, C.; Dizdar, K.C.; Dispinar, D. Investigation of Effect of Conformal Cooling Inserts in High-Pressure Die Casting of $AlSi_9Cu_3$. *Int. J. Adv. Manuf. Technol.* **2022**, *121*, 7311–7323. [CrossRef]
39. Liu, Q.; Liu, M.; Xu, C.; Xiao, W.; Yamagata, H.; Xie, S.; Ma, C. Effects of Sr, Ce and P on the Microstructure and Mechanical Properties of Rapidly Solidified Al–7Si Alloys. *Mater. Charact.* **2018**, *140*, 290–298. [CrossRef]
40. Okayasu, M.; Takeuchi, S. Crystallization Characteristics of Cast Aluminum Alloys during a Unidirectional Solidification Process. *Mater. Sci. Eng. A* **2015**, *633*, 112–120. [CrossRef]
41. Iwata, Y.; Dong, S.; Sugiyama, Y.; Iwahori, H. Effects of Solidification Behavior during Filling on Surface Defects of Aluminum Alloy Die Casting. *Mater. Trans.* **2013**, *54*, 1944–1950. [CrossRef]
42. Liao, H.C.; Zhang, M.; Bi, J.J.; Ding, K.; Xi, X.; Wu, S.Q. Eutectic Solidification in Near-Eutectic Al-Si Casting Alloys. *J. Mater. Sci. Technol.* **2010**, *26*, 1089–1097. [CrossRef]
43. Hsu, Q.C.; Do, A.T.; Yeh, K.C.; Ye, J.H. Improvement on Die-Casting Efficiency and Property of Aluminum Alloy Casing. *Key Eng. Mater.* **2015**, *625*, 518–524. [CrossRef]